# Crystallinity Evaluation and Dislocation Observation for an Aluminum Nitride Single-Crystal Substrate on a Wafer Scale

YONGZHAO YAO [ID],[1,3] YOSHIHIRO SUGAWARA,[1] YUKARI ISHIKAWA,[1] NARIHITO OKADA,[2] and KAZUYUKI TADATOMO[2]

1.—Japan Fine Ceramics Center, 2-4-1 Mutsuno, Atsuta, Nagoya 456-8587, Japan. 2.—Yamaguchi University, 2-16-1 Tokiwadai, Ube, Yamaguchi 755-8611, Japan. 3.—e-mail: y_yao@jfcc.or.jp

The crystallinity of a 35-mm-diameter AlN single-crystal substrate grown by physical vapor transport was investigated using x-ray diffraction and Raman spectral mapping. Dislocations in the same sample were observed using an etch pit method, synchrotron x-ray topography, and transmission electron microscopy. The central area of a diameter of 25 mm was featured with high crystallinity and high uniformity, whereas the rim area showed degradation in crystallinity. An improvement in the radius of curvature was confirmed along the growth direction of $[000\bar{1}]$. The dislocations were revealed as etch pits, and the position-dependent etch pit density was analyzed across the whole wafer. Transmission electron microscopy showed that under the current chemical etching condition, the size of the etch pits in the $[11\bar{2}0]$ diagonal direction was approximately linearly proportional to the magnitude of the Burgers vectors, and therefore could be used to classify dislocations.

**Key words:** Aluminum nitride, x-ray diffraction, dislocation, synchrotron x-ray topography, Raman, etch pit method, transmission electron microscopy

## INTRODUCTION

The superior physical properties of aluminum nitride (AlN), such as an ultra-wide direct bandgap, high breakdown voltage, and high thermal conductivity, have made this material one of the most promising candidates for the application of short-wavelength optoelectronic devices for deep ultraviolet (DUV) light-emitting and power-switching electronic devices capable of operating at high voltage, high frequency, and elevated temperature.[1–4] To realize the optoelectronic and electronic devices that can fully exploit the physical properties of AlN, free-standing AlN substrates with a large diameter, high

crystallinity, high uniformity, and low dislocation density are required, on which active layers will be grown.

Crystal growth of AlN boules or thick layers using various growth techniques has been reported, including solution growth,[5,6] elementary source vapor phase epitaxy,[7] hydride vapor phase epitaxy (HVPE),[8–11] and physical vapor transport (PVT).[12–20] Annealing of AlN templates grown by sputtering has recently been reported as a potential technique for providing high-quality AlN substrates.[21–23] Among the above growth techniques, PVT has an advantage over the other methods in terms of growth rate and structural quality. Single-crystal AlN substrates fabricated using PVT are commercially available.[24]

The position-dependent crystallinity and dislocation distribution across a wafer provide important feedback for the optimization of growth conditions.

These pieces of information are also essential for the design of subsequent processes such as epitaxial growth and device fabrication. In this work, we have carried out a comprehensive evaluation on an up-to-date commercial AlN substrate using x-ray diffraction (XRD), Raman spectral mapping, the etch pit method, transmission electron microscopy (TEM), and synchrotron x-ray topography (XRT). Particular attention has been paid to the position dependence of substrate quality and dislocation density. Evaluations on two opposite polar faces, namely the front and backside of the substrate, were also compared to investigate the evolution of structural properties along the growth direction of [000$\bar{1}$].

## EXPERIMENTAL DETAILS

The sample evaluated in this work was a commercial AlN single-crystal substrate (HexaTech, Inc.[24]) grown by PVT. It was 35 mm in diameter and 550 $\mu$m in thickness. Both the Al-polar and the N-polar surfaces were treated to obtain an epi-ready finish using chemical–mechanical polishing (CMP). The crystallinity, lattice constants, and radius of curvature of the substrate were evaluated using a PANalytical Empyrean high-resolution XRD platform at room temperature of 25 $\pm$ 1°C. A Ge(220) symmetric four-crystal monochromator was applied on the incident side, and a three-bounce symmetric analyzer or a PIXcel[3D] two-dimensional (2D) solid-state hybrid pixel detector[25] was used on the detection side. The wavelength of the x-ray source was 0.154060 nm. By carefully positioning the sample in the diffractometer[26,27] and calibrating the zero point of 2$\theta$ of the three-bounce symmetric analyzer, precision of $1 \times 10^{-5}$ in lattice constants was achieved in this system. Raman spectral mapping in the back-scattering geometry was performed using a JASCO NRS-7100 confocal laser Raman spectrometer with a Nd:YVO$_4$ laser ($\lambda$ = 532.5 nm) as the excitation source. The spectral resolution under the present measurement conditions was approximately 0.2 cm$^{-1}$ in wavenumber. The atomic lines of a neon lamp and a standard silicon crystal were used as the references to calibrate the Raman spectra. To reveal the dislocations from the substrate surface, chemical etching in molten KOH + Na$_2$O$_2$ was carried out at 520°C for 6 min, and the etch pits were observed using a laser microscope. The cross-sectional TEM specimens were then fabricated by cutting out 150-nm-thick slabs containing the target dislocation segments using a focused ion beam (FIB). The TEM observation was performed on a JEOL JEM-2010 DM using large-angle convergent-beam electron diffraction (LACBED) to determine the Burgers vectors of dislocation. The observation of dislocations using synchrotron XRT was carried out prior to the chemical etching at beamlines BL-3C and BL-14B of the Photon Factory at High Energy Accelerator Research Organization (KEK-PF), Tsukuba, Japan. The monochromatic

x-ray with a wavelength of 0.0893 nm ($E$ = 13.9 keV) was irradiated to the sample surface at an incident angle of 5°. The topographic images at $g = 22\bar{4}6$ were recorded on nuclear emulsion plates.[28,29]

## RESULTS AND DISCUSSION

Figure 1a and b show the position-dependent 0004 $\omega$ rocking curves ($\omega$-RCs) measured from the Al-polar and the N-polar surfaces, respectively. The center of the substrate was set to 0 mm. A PIXcel[3D] detector in open detector mode[25] was used for these measurements, which allowed the diffracted x-ray from the sample to be collected simultaneously over a 2$\theta$ range of several degrees. Therefore, the peak positions of the $\omega$-RCs indicated the direction of the
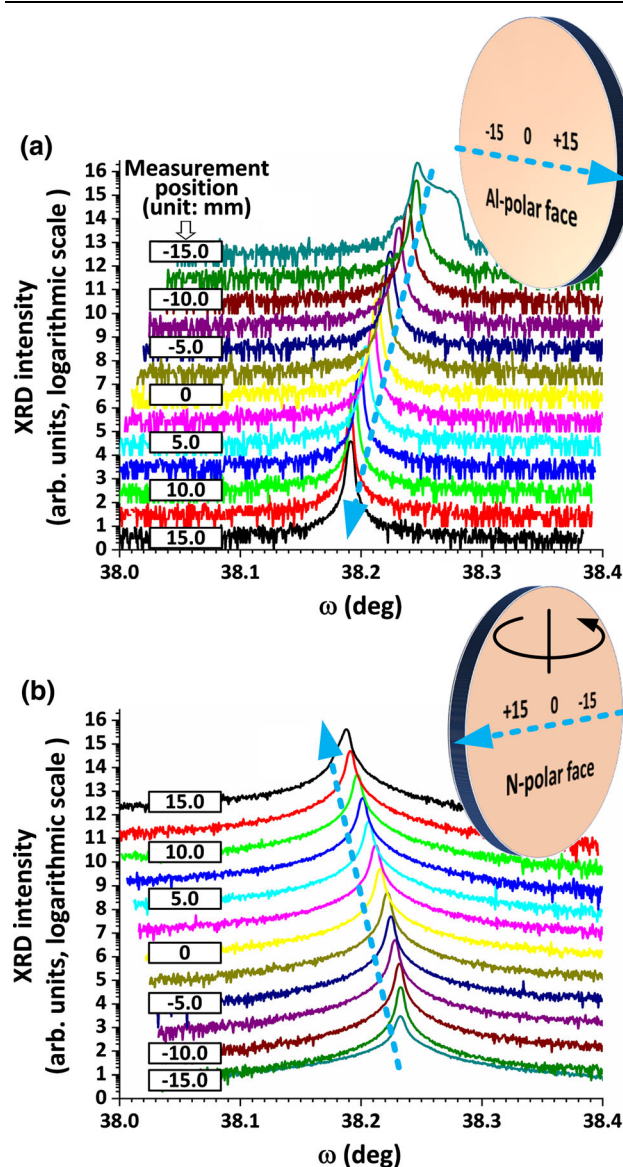


Fig. 1. Position-dependent XRD $\omega$ rocking curves measured from (a) the Al-polar face and (b) the N-polar face. The substrate was rotated around the vertical line in the figure from one polar face to the other.

0004 normal at each measurement position. By applying linear fitting to these peak positions as a function of the measurement position, the radius of curvature ($R_c$) of the $c$-planes was calculated to be around 30 m from the Al-polar face. The $R_c$ measured from the N-polar face was several meters greater than that measured from the Al-polar face, which is in agreement with our previous study on another AlN substrate grown under similar conditions.[29] The $c$-planes were bent towards the [000$\bar{1}$] direction, namely, the $c$-planes were convex-shaped when viewed from the N-polar face. This is consistent with the fact that the convex thermal field was applied to the growth front during the N-polar growth.[14,20] This convex thermal field is thought to be crucial to achieving a large expansion angle during PVT growth to enable a controlled diameter enlargement.[17,18,20] The increase in the $R_c$ from the Al-polar to the N-polar face indicates an improvement in terms of the release of thermal stress during the PVT growth along the [000$\bar{1}$] direction.[17]

Figure 2 shows the XRD intensity and full-width at half-maximum (FWHM) of the $\omega$-RCs as a function of the measurement position. The central area within a 25-mm-diameter range showed highly uniform crystallinity. Small standard deviations of $\delta_{PI} = 1.7\%$ for the peak intensity and $\delta_F = 0.7\%$ for the FWHM were calculated from the Al-polar face, and those for the N-polar face were $\delta_{PI} = 0.8\%$ and $\delta_F = 2.1\%$. On the other hand, the 5-mm-wide rim of the substrate showed a notable degradation in crystallinity. As shown in Fig. 1, a significant peak broadening or the presence of a peak shoulder was confirmed from the $\omega$-RCs at 15.00 mm and $-15.0$ mm for both polar faces. This suggests a relatively large misorientation of the $c$-plane normal, namely tilt of the $c$-axis, in the rim area in comparison with the central area. For seeded PVT growth of large AlN boules, diameter enlargement
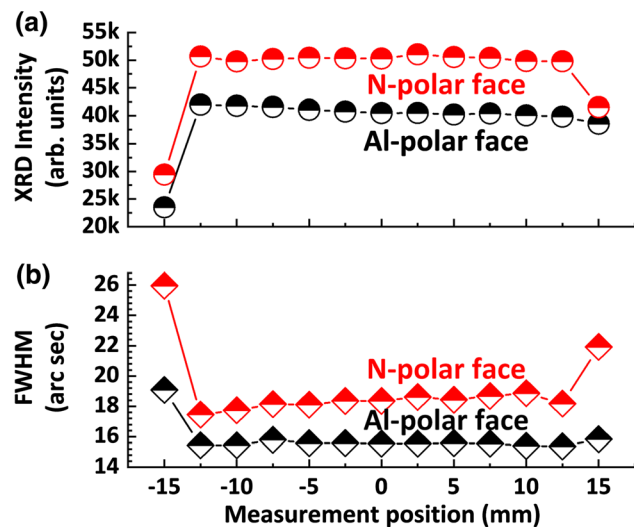
from the original size of the seed is important, which is normally achieved by the lateral growth of the crystal on the prismatic $m\{1\bar{1}00\}$ facets or pyramidal $\{1\bar{1}0n\}$ facets,[14,16–18,20] while the central area of the substrate is expected to be dominated by the (000$\bar{1}$) N-face growth. The above position-dependent XRD measurements imply that it is important to match the crystal orientation of the $m\{1\bar{1}00\}$ and $\{1\bar{1}0n\}$ growth with that of the (000$\bar{1}$) N-face growth to improve the uniformity across the entire wafer and increase the usable area.

Comparing the XRD intensities between the two polarities, an average 23% increase from the Al-polar to the N-polar face was confirmed, suggesting an improvement in crystallinity along the growth direction of [000$\bar{1}$]. However, a broadening of the FWHM was observed from an average of 15.5 arcsec for the Al-polar face to an average of 18.3 arcsec for the N-polar face. The reason for the broadening is not clear so far. A possible explanation is related to the difference in surface treatment by CMP, taking into consideration that the chemical reactivity of two opposite polarities differs significantly.

Figure 3 shows the XRD reciprocal space maps (RSMs) near the symmetric 0004 and asymmetric 01$\bar{1}$5 reflections, recorded from the substrate center of the Al-polar and the N-polar face, respectively. A three-bounce symmetric analyzer was used on the detector side instead of the above-mentioned PIXcel$^{3D}$ detector to ensure a high angular resolution of $2\theta$. The substrate showed very high crystal perfection in terms of great lateral coherence length and small tilt and twist components, as indicated by the small RSM FWHM for both symmetric and asymmetric reflections.[30,31] $\omega$-RC and $\omega/2\theta$ scans (not shown) at the 0004 and 01$\bar{1}$5 reflections had FWHM in the range of 6.9–21.2 arcsec (Table I). The N-polar face showed a slight broadening of the RSM contour compared with the Al-polar face, but it is noted that these broadened contour lines correspond to weak reflections with an intensity lower than 1% of the contour peak. This broadening was tentatively attributed to the residual strain in the topmost N-polar surface introduced by the CMP treatment.

$\omega/2\theta$ scans recorded at 0004 and 01$\bar{1}$5 reflections were used to determine the lattice constants $c$ and $a$, respectively. The substrate center and four positions 10 mm from the center were measured on each polar face, to analyze the variation in lattice constants along the growth direction and within the $c$-plane. $c_0 = 0.498089$ nm and $a_0 = 0.311197$ nm were adopted from Paszkowicz et al.[32] as the strain-free lattice constants of AlN. Figure 4 shows the strain component $\Delta c/c_0$ and $\Delta a/a_0$ at five measurement points as the deviation of the measured lattice constants with respect to the reference. Lattice constants $c$ measured at all points were smaller than the reference, whereas lattice constants $a$ were greater than the reference. The
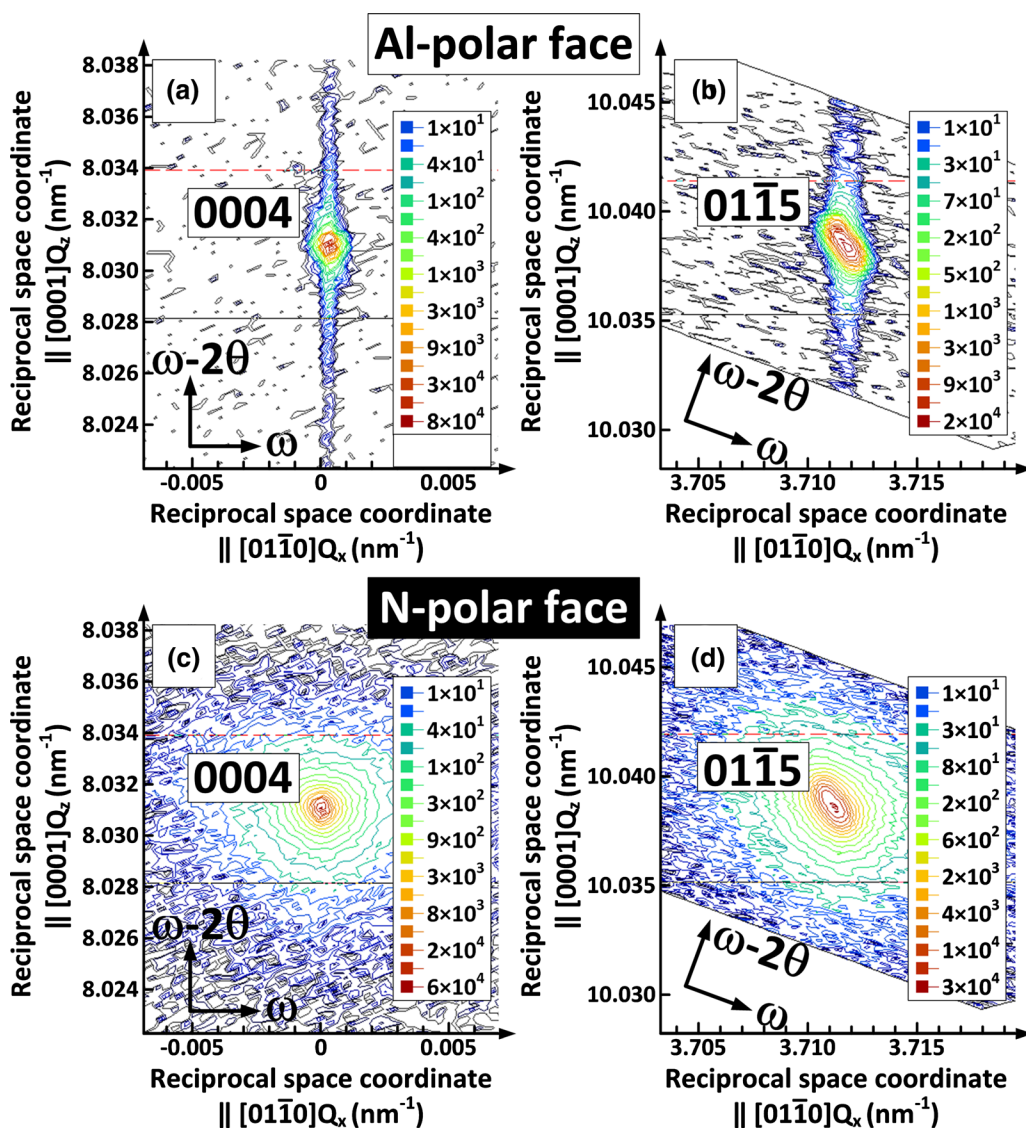


Fig. 2. (a) XRD intensity and (b) FWHM of $\omega$ rocking curves as a function of the measurement position, measured from the Al-polar face (black) and the N-polar face (red) (Color figure online).

Fig. 3. XRD reciprocal space maps (RSMs) near symmetric 0004 and asymmetric 01$\bar{1}$5 reflections, acquired from the substrate center. (a, b) The Al-polar and (c, d) the N-polar face. RSMs near both the symmetric and asymmetric reflections show broadening mainly in the direction perpendicular to the diffraction vector.

**Table I. FWHM of XRD $\omega/2\theta$ scan and $\omega$ rocking curve of the symmetric 0004 and asymmetric 01$\bar{1}$5 reflections**

| Reflections | Scan mode | Al-polar face (arcsec) | N-polar face (arcsec) |
|---|---|---|---|
| 0004 | $\omega$-RC | 6.9 | 9.2 |
| | $\omega/2\theta$ | 7.2 | 12.1 |
| 01$\bar{1}$5 | $\omega$-RC | 17.2 | 19.4 |
| | $\omega/2\theta$ | 17.4 | 21.2 |

deviation of lattice $a$ was several parts in $10^{-5}$. The volume of unit cell calculated using the measured lattice constants was nearly constant for all measurement points, but the nature of strain seemed not to be completely biaxial assuming a Poisson ratio of 0.203[33] for AlN. Focusing on the in-plane variation of the lattice constants, it was found that the substrate center had a very small deviation from

the reference values,[32] while this deviation increased towards the periphery. Comparing the lattice constants measured from the front and backside of the substrate, which represent different growth stages 550 $\mu$m apart from each other in the $\langle 0001 \rangle$ direction, it was notable that the lattice constants (both $c$ and $a$) slowly approached the strain-free values along the [000$\bar{1}$] direction, i.e., the
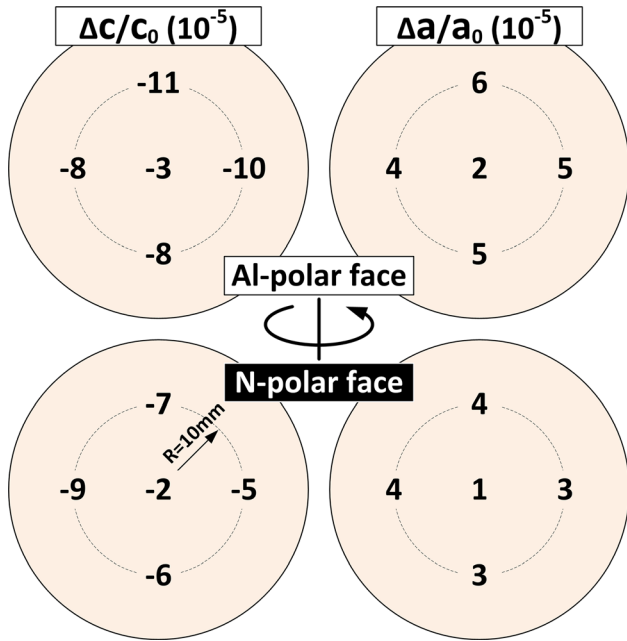
Fig. 4. Deviation of the measured lattice constants from the reference values.[32] Upper: Al-polar face. Lower: N-polar face.

growth direction of the AlN ingot. This might be related to the fact that the later stage of the growth was carried out under reduced stress.[17] Other factors affecting the lattice constants such as the impurity incorporation and the curvature of crystal planes need to be taken into consideration to clarify the characteristics of the strain.

To further investigate the distribution of residual stress and the crystallinity, Raman spectral mapping was carried out. Figure 5a shows the representative Raman spectrum recorded from the N-polar face under scattering geometry $k_i(e_i, -)k_s$,[34] where $k_i = [0001]$, $k_s = [000\bar{1}]$, and $e_i = \langle 11\bar{2}0 \rangle$. $E_2$(high) was the strongest phonon mode allowed under this geometry, and it peaked at 656.6 cm$^{-1}$ as determined using a Voigt fitting. In addition, $E_1$(TO) and $A_1$(LO) phonon modes were observed. FWHM maps of the $E_2$(high) peak measured from the Al-polar and the N-polar faces are shown in Fig. 5b and c, respectively. The average FWHM of 400 measured points across the whole substrate was 3.4 cm$^{-1}$ (standard deviation $\delta = 1.6\%$) for the Al-polar face and 3.3 cm$^{-1}$ ($\delta = 2.8\%$) for the N-polar face. The small FWHM of the $E_2$(high) and its high uniformity across the substrate is a good indicator of the high structural quality and low impurity incorporation. FWHM of 3–4 cm$^{-1}$ have been reported for high-quality single-crystal AlN bulk,[16,35] whereas AlN films fabricated on foreign substrates typically have wider FWHM,[36–39] presumably due to the crystallinity degradation caused by lattice mismatch and in some cases by the incorporation of impurities such as oxygen.[38] The maps of the $E_2$(high) peak positions measured from the Al-polar
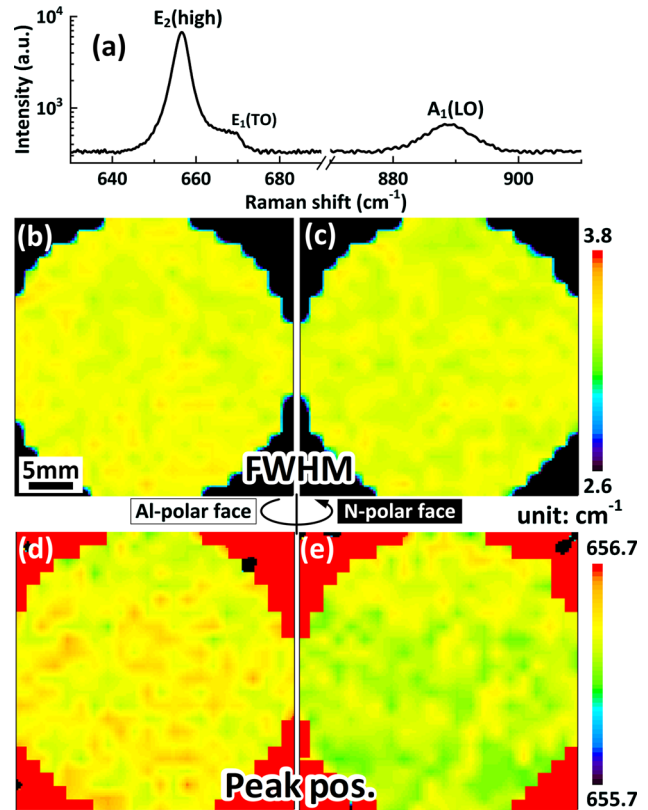


Fig. 5. (a) Raman spectrum measured from the substrate center of the N-polar face. (b, c) Maps of the FWHM of $E_2$(high) phonon mode, from the Al-polar and the N-polar face, respectively. (d, e) Maps of the peak position of $E_2$(high) phonon mode, from the Al-polar and the N-polar face, respectively. The scale bar is 5 mm and it applies to all four Raman maps in (b–e).

and the N-polar faces are shown in Fig. 5d and e, respectively. Note that the wavenumber scale bar is 1 cm$^{-1}$ ranging between 655.7 cm$^{-1}$ and 656.7 cm$^{-1}$, suggesting a uniform distribution of stress at least at the detection limit of Raman spectra. Yang et al.[39] reported a biaxial stress coefficient of the $E_2$(high) peak around −4.04 cm$^{-1}$/GPa, while other experiments[36–38] and theoretical calculations[40] suggested a slightly smaller value in the range of −2.55 to −3.7 cm$^{-1}$/GPa. Using these values in the literature, we estimated that the Raman peak would have a shift no greater than 0.2 cm$^{-1}$ if the normal strain component $\varepsilon_{xx} = \Delta a/a$ was smaller than 10$^{-4}$. This is in agreement with the lattice constants measured by XRD as mentioned above. The peak position averaged on 400 measured points across the whole substrate was 656.4 cm$^{-1}$ and 656.3 cm$^{-1}$ for the Al-polar and the N-polar faces, respectively, which indicated that the compressive stress was slowly released along the growth direction of [000$\bar{1}$].

Next, we investigated the dislocations in the substrate, including the dislocation density, dislocation types, and their distribution across the substrate. Figure 6a, b, c, d, and e show the representative etch pit images observed from the
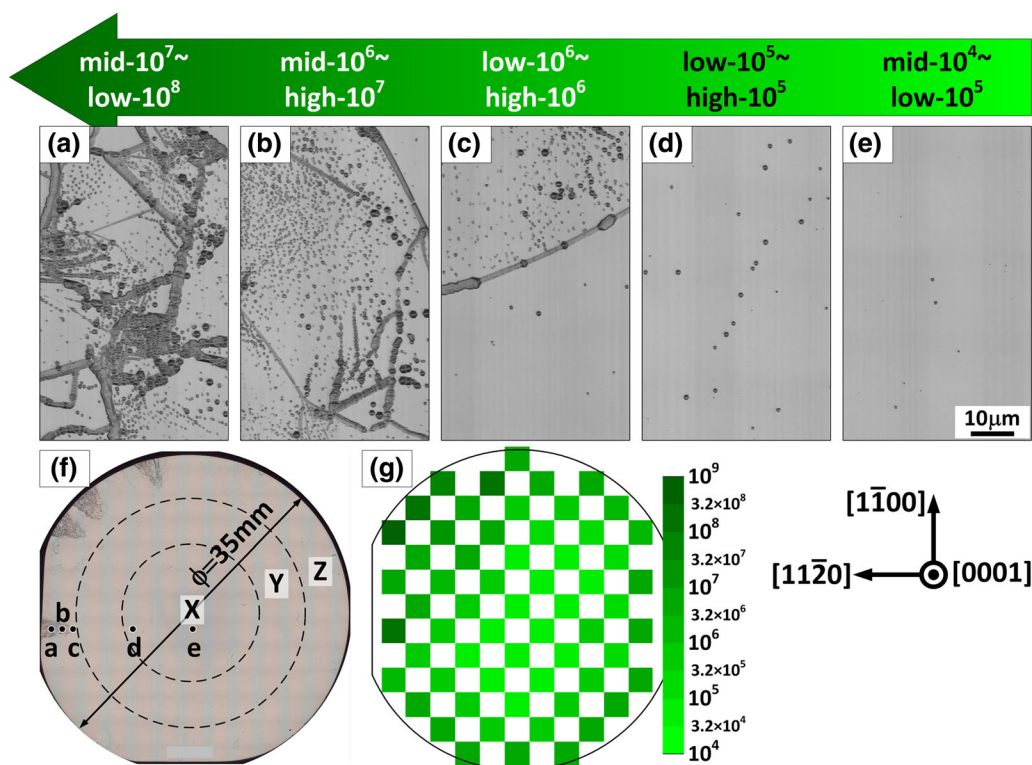
Fig. 6. (a–e) Typical etch pit images taken from the Al-polar face after chemical etching. Their positions are shown in (f) the image of the entire substrate. (g) The position-dependent etch pit density (EPD). Note that these values are not the average EPD over each $2.7 \times 2.7$ mm$^2$ square area, but were calculated using a representative etch pit image taken from the center of each square. The scale bar is 10 $\mu$m and it applies to images in (a–e).

Al-polar face after chemical etching. The entire substrate is divided into three regions: region X at the center with a radius of 7.5 mm, and two 5-mm-wide rings, regions Y and Z, as shown in Fig. 6f. The lowest etch pit density (EPD) around mid-$10^4$ cm$^{-2}$ was observed near the substrate center. Almost all etch pits formed in this area were hexagonal-shaped, indicating that they corresponded to threading dislocations. Moving away from the center, the average EPD increased by more than one order of magnitude to high-$10^5$ cm$^{-2}$ near the edge of region X, and it gradually increased to low-$10^6$ cm$^{-2}$ across region Y. Seashell-shaped pits, which were related to the basal plane dislocations (BPDs), started to appear and increased in number towards the periphery. Region Z was featured with further increasing EPD, over a range of low-$10^6$ cm$^{-2}$ to low-$10^8$ cm$^{-2}$. A large number of etch pits comprising arrays at the low-angle grain boundaries (LAGBs) were observed (Fig. 6a and b).[14] An optical image of the whole substrate after etching is shown in Fig. 6f, where only pit arrays or clusters at a density higher than mid-$10^7$ cm$^{-2}$ were visible at this low magnification. The map of EPD across the substrate is shown in Fig. 6g. The position dependence of the EPD (lowest at the center and increased towards the periphery) showed a similar tendency as the strain distribution as presented in Fig. 4, indicating a close correlation
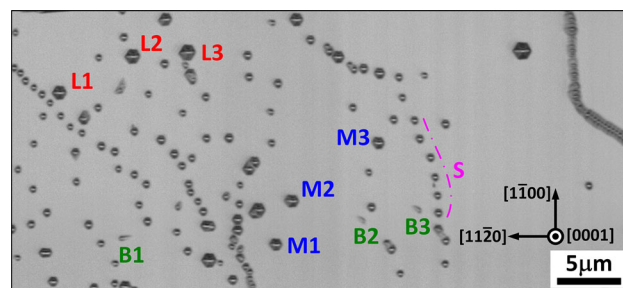
between dislocation formation and residual stress. This result emphasizes the importance of carefully controlling the stress distribution during PVT growth to reduce dislocations.

We next discuss the classification of dislocations by the shapes and sizes of the etch pits. Figure 7 shows a representative etch pit image with an EPD higher than $10^7$ cm$^{-2}$. Four types of etch pits were able to be classified: S (small), M (medium), and L (large) hexagonal pits and seashell-shaped pits (labeled "B" for BPDs). The average size ratio of hexagonal etch pits was S:M:L = 1.0:1.5:1.9. The Burgers vector of dislocations under each type of



Fig. 7. Etch pit image taken from an area containing S (small), M (medium), and L (large) hexagonal pits and the seashell-shaped pits (labeled "B" for BPDs). Numbers 1–3 indicate several examples in each type.

etch pit was identified using the TEM observation in LACBED mode.[41] Figure 8 shows an example of S-pit identification. When the dislocation line under an S-pit was superimposed on the Laue reflection line of $g = \bar{2}\bar{2}40$ ($g$ is the reciprocal lattice vector), the latter showed a split of $n = +2$ (Fig. 8a). Similarly, the splits of $g = 22\bar{4}\bar{2}$ and $g = \bar{3}\bar{2}5\bar{5}$ Laue lines were $n = -2$ and $n = +3$, respectively (Fig. 8b and c), when the dislocation line was superimposed. According to the relationship of $g_{hkil} \cdot b_{uvtw} = n$, where $b$ is the Burgers vector of the dislocation, the following equations can be written:

$$\begin{cases} -2u - 2v + 4t = 2 \\ 2u + 2v - 4t - 2w = -2 \\ -3u - 2v + 5t - 5w = 3 \\ u + v + t = 0 \end{cases} \quad (1)$$

Therefore, the Burgers vector of the dislocation under this S pit can be identified as $b = \frac{1}{3}[\bar{2}110]$. It is well known that the size of etch pit is mainly determined by the magnitude rather than the direction of the Burgers vector; thus it is reasonable to attribute all pure edge-type dislocations with equivalent $b = \frac{1}{3}\langle 11\bar{2}0 \rangle$ to the S pits. Similarly, the LACBED observations indicated that the M pits corresponded to the screw-type dislocations with $b = \langle 0001 \rangle$. and the L pits corresponded to the mixed-type dislocations with $b = \langle 0001 \rangle + \frac{1}{3}\langle 11\bar{2}0 \rangle$ (so-called $c + a$ dislocation) or edge-type dislocations with $b = \frac{2}{3}\langle 11\bar{2}0 \rangle$ (2a edge-type dislocation) in some cases (Table II). Under the chemical etching conditions used in this study, the size of the hexagonal

etch pits in the $[11\bar{2}0]$ diagonal direction was approximately linearly proportional to the magnitude of the Burgers vectors of the threading dislocations. Furthermore, the LACBED observations confirmed that the seashell-shaped pits corresponded to the BPDs with $b = \frac{1}{3}\langle 11\bar{2}0 \rangle$. Both screw-type BPDs with $b // \zeta$ ($\zeta$ is the direction of dislocation line) and mixed-type BPDs with $b$ forming a 60° angle with $\zeta$ were found.

Based on the above assignment, we were able to analyze the distribution of dislocation types across the substrate. It was found that the threading dislocations were overwhelmingly dominant, and a low percentage ($< 3\%$) of BPDs were found in region X. However, it should be pointed out that the etch pit method only reveals dislocations that have emerged at the surface; therefore, the proportion of BPDs might vary with depth. Previous XRT observation has suggested that some BPDs converted to threading dislocations near the sample surface.[29] Elementary edge-type with $b = \frac{1}{3}\langle 11\bar{2}0 \rangle$ (i.e., S-pits) constituted about 95% of the threading dislocations. Across region Y, the percentage of BPDs gradually increased from $< 3\%$ to about 7%, but the elementary edge-type threading dislocations remained dominant, as in region X. In region Z, the proportion of BPDs increased significantly, reaching nearly 15% in the areas with a dislocation density of high-$10^7$ cm$^{-2}$. The increased BPD density might have been caused by the large thermal stress in the rim area. Another feature of region Z was the significantly increasing percentage of etch pits with sizes larger than the S-pits, especially in the areas
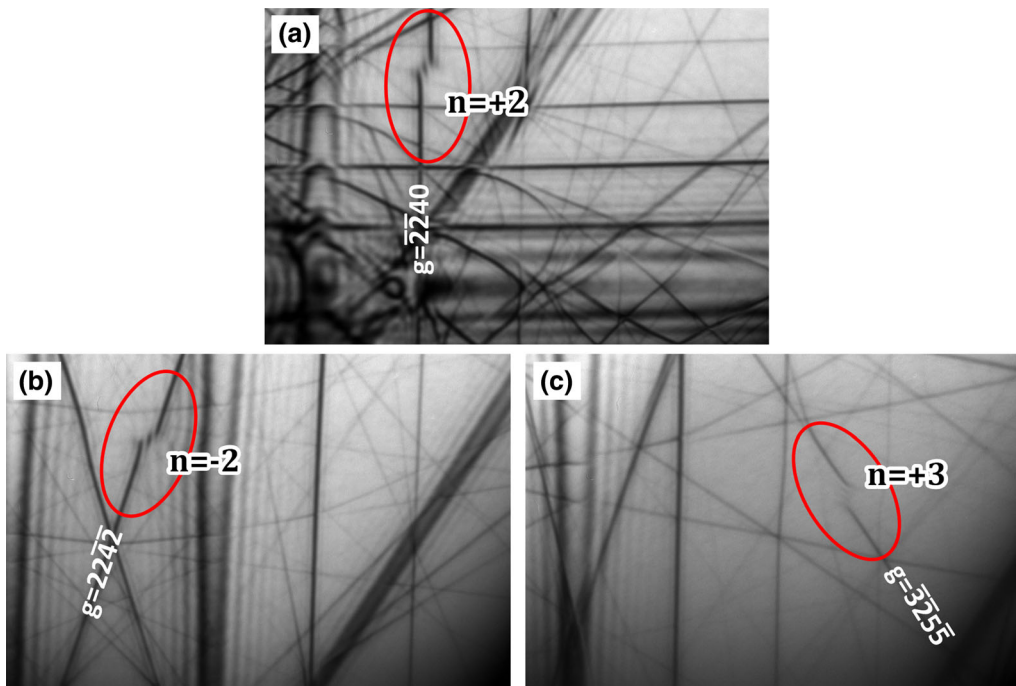


Fig. 8. LACBED pattern of the dislocation under an S-pit, superimposed with the Laue reflection lines of (a) $g = \bar{2}\bar{2}40$, (b) $g = 22\bar{4}\bar{2}$, and (c) $g = \bar{3}\bar{2}5\bar{5}$. $g$ is the reciprocal lattice vector. The split of the Laue reflection lines is marked by a red circle in each image (Color figure online).

**Table II. Size levels of three types of hexagonal etch pits and the corresponding Burgers vector of dislocation under these types of etch pits**

| Size levels of hexagonal etch pits | Small | Medium | Large |
|---|---|---|---|
| Pit size ($\mu$m) ([11$\bar{2}$0] diagonal length) | 0.69 | 1.02 | 1.33 |
| Size ratio (define small as 1) | 1.0 | 1.5 | 1.9 |
| Burgers vector, $b$ | $a$ (edge-type) | $c$ (screw-type) | $c + a$ (mixed-type) $2a$ (edge-type) |
| Magnitude of $b$ (nm) | 0.311 | 0.498 | 0.587 0.622 |
| Burgers vector ratio (define $a$ as 1) | 1.0 | 1.6 | 1.9 2.0 |

with high EPD. As a result, the S-pits reduced to below 70% of all hexagonal pits. In addition, the clear classification of size levels S, M, and L observable in regions X and Y was no longer available in region Z. Instead, a continuous distribution of pit size was observed. These results indicate that there were serious dislocation interaction and dislocation inclination (with respect to the $c$-axis) in this high-EPD area.[42] The interaction between dislocations is a possible mechanism of the generation of dislocations with larger Burgers vectors, which led to larger etch pits. Another possible reason for the continuous distribution of pit size is the inclination of threading dislocations.[42] As an estimation, assuming that the bottom of an etch pit formed at a threading dislocation was 2 $\mu$m deep from the original sample surface, an inclination angle of 20°[42] towards the $\langle 11\bar{2}0 \rangle$ direction would result in an enlargement of pit size by 2 $\mu$m $\times$ tan20° = 0.73 $\mu$m. The inclination of threading dislocations might have occurred as a combined result of several factors, including the curved crystal planes, dislocation interaction, impurity incorporation, and the crystal growth on prismatic or pyramidal facets. It is considered that all these factors become more significant in the rim area than at the substrate center.

XRT is a nondestructive technique used to observe dislocations in AlN. Figure 9 shows the XRT images taken from both sides of the substrate, which can be used to study the dislocation propagation behavior. Figure 9a and b are from the same area near the substrate center. The information on the x-ray penetration depth is necessary to explain the dislocation contrast in the XRT images, and it was estimated using the wavelength-dependent linear absorption coefficient of AlN.[43,44] The result is shown in Table III, with a comparison with the penetration depths in the XRD measurements.

The white spot-like contrasts correspond to threading dislocations propagating parallel to the $c$-axis. As the x-ray had a large penetration depth of about 87.2 $\mu$m in AlN, any threading dislocations with notable inclination will lead to line-shaped contrasts on the projection plane (i.e., the emulsion
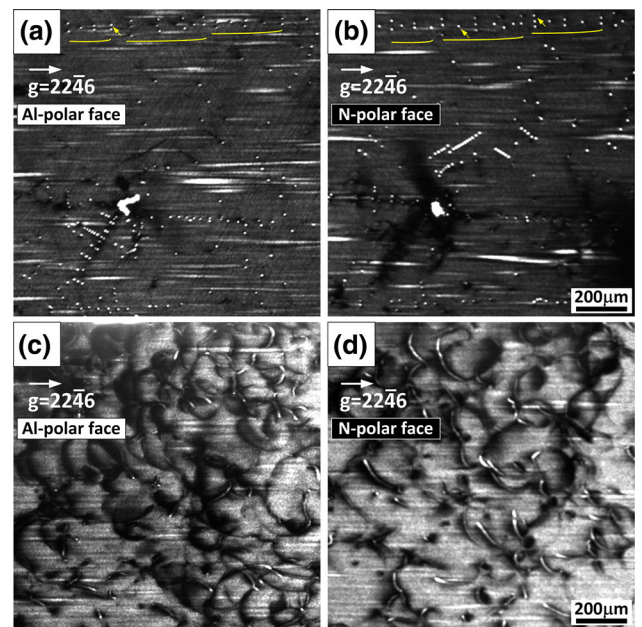


Fig. 9. XRT images of (a, b) the same area near the substrate center, where the threading dislocations propagating parallel to the $c$-axis dominate, taken from the Al-polar and the N-polar face, respectively. XRT images of (c, d) the same area near the boundary of regions Y and Z, which represents a highly defective region dominated by BPDs and inclined threading dislocations, taken from the Al-polar and the N-polar face, respectively. The images of the N-polar face have been horizontally flipped from the original images in order to correlate with the images of the Al-polar face. All four images share the same scale bar of 200 $\mu$m.

plate) rather than spot-like contrasts. Comparing Fig. 9a with b, although the overall dislocation density did not change significantly from the Al-polar face to the N-polar face, there was no exact one-to-one correlation of the emerging positions of dislocation from the two sides. For example, as indicated by the yellow arrows (upper part of Fig. 9a and b), some threading dislocations that had only emerged from one side of the substrate were confirmed. It was considered that they were threading dislocations converted from BPDs or converted to BPDs during the crystal growth. On the other hand, the three horizontal yellow lines in the same area mark some of the threading dislocations that have a

**Table III. Parameters of XRD and XRT observations and the x-ray penetration depth of in the AlN single-crystal substrate, which was defined as the absorption depth and calculated using the equations reported in Ishiji et al.[43]**

| Evaluation method | Reciprocal lattice vector, $g$ | X-ray wavelength, $\lambda$ (nm) | Incident angle, $\alpha$ (°) | Bragg angle, $\theta_B$ (°) | Absorption coefficient, $\mu$ (cm$^{-1}$)[44] | Penetration depth, $d_p$ ($\mu$m)[a] |
|---|---|---|---|---|---|---|
| XRT | $22\bar{4}6$ | 0.0893 | 5.01 | 51.86 | 21.17 | 87.2 |
| XRD | 0004 | 0.15406 | 38.22 | 38.22 | 111.44 | 63.9 |
| XRD | $01\bar{1}5$ | 0.15406 | 35.24 | 55.52 | 111.44 | 74.7 |

[a]Penetration depth is defined as the point where the diffracted intensity of x-rays reduces to 10% of the incident intensity.

good correlation in location between two faces, suggesting that these dislocations were parallel to the c-axis. Figure 9c and d are from the same area near the boundary of regions Y and Z, which represented a highly defective region. In comparison with the spot-like contrasts at the substrate center, line-shaped and arc-shaped contrasts dominated this area, indicating a large amount of BPDs and inclined threading dislocations. The arc-shape of the BPD-related contrast, which resembles the case of 4H-SiC,[45–49] indicates that BPDs in AlN might bend or glide under stress. Similar to the substrate center, the dislocation density in this area did not change significantly from the Al-polar to the N-polar face. Dislocation density calculated from the XRT images is in reasonable agreement with that estimated from EPD.

## CONCLUSIONS

AlN is a promising wide-bandgap semiconductor for next-generation optoelectronic and power devices. In this work, we characterized the crystallinity of a 35-mm-diameter AlN single-crystal substrate grown by PVT. XRD intensity and FWHM indicated that the central area of a 25-mm diameter had high crystallinity and high uniformity. The radius of curvature of the c-planes was about 30 m, and it was convex-shaped viewed from the N-polar side. An improved curvature and reduced stress along the growth direction of [000$\bar{1}$] were observed. This was consistent with the results of lattice constants measured by XRD. Raman spectral mapping showed small FWHM about 3.3–3.4 cm$^{-1}$ of the Raman $E_2$(high) phonon mode for both polar faces, and the FWHM was uniform across the entire substrate. Stress distribution was also uniform, as indicated by the maps of the $E_2$(high) peak position.

Dislocations were revealed using chemical etching, and dislocations under each type of etch pit were identified using TEM. The size of the etch pits in the [11$\bar{2}$0] diagonal direction was approximately linearly proportional to the magnitude of the Burgers vectors. From the substrate center to the rim area, the dislocation density increased from

low-10$^4$ cm$^{-2}$ to low-10$^8$ cm$^{-2}$, where threading dislocations and BPDs appeared as dislocation arrays and clusters. The proportion of edge-type and screw-type threading dislocations and BPDs exhibited a radial position dependence. XRT observations showed a high possibility of conversion between threading dislocations and BPDs.

## REFERENCES

1. S.J. Pearton, J.C. Zolper, R.J. Shul, and F. Ren, *J. Appl. Phys.* 86, 1 (1999).
2. S.C. Jain, M. Willander, J. Narayan, and R. Van Overstraeten, *J. Appl. Phys.* 87, 965 (2000).
3. B. Monemar, P.P. Paskov, J.P. Bergman, A.A. Toropov, and T.V. Shubina, *Phys. Status Solidi A* 244, 1759 (2007).
4. H. Amano, Y. Baines, E. Beam, M. Borga, T. Bouchet, P.R. Chalker, M. Charles, K.J. Chen, N. Chowdhury, R. Chu, C. De Santi, M.M. De Souza, S. Decoutere, L. Di Cioccio, B. Eckardt, T. Egawa, P. Fay, J.J. Freedsman, L. Guido, O. Häberlen, G. Haynes, T. Heckel, D. Hemakumara, P. Houston, J. Hu, M. Hua, Q. Huang, A. Huang, S. Jiang, H. Kawai, D. Kinzer, M. Kuball, A. Kumar, K.B. Lee, X. Li, D. Marcon, M. März, R. McCarthy, G. Meneghesso, M. Meneghini, E. Morvan, A. Nakajima, E.M.S. Narayanan, S. Oliver, T. Palacios, D. Piedra, M. Plissonnier, R. Reddy, M. Sun, I. Thayne, A. Torres, N. Trivellin, V. Unni, M.J. Uren, M. Van Hove, D.J. Wallis, J. Wang, J. Xie, S. Yagi, S. Yang, C. Youtsey, R. Yu, E. Zanoni, S. Zeltner, and Y. Zhang, *J. Phys. D Appl. Phys.* 51, 163001 (2018).
5. K. Kamei, Y. Shirai, T. Tanaka, N. Okada, A. Yauchi, and H. Amano, *Phys. Status Solidi C* 4, 2211 (2007).
6. S. Watanabe, M. Nagaya, Y. Takeuchi, K. Aoyagi, S. Harada, M. Tagawa, and T. Ujihara, *Mater. Sci. Forum* 858, 1210 (2016).
7. P. Wu, M. Funato, and Y. Kawakami, *Sci. Rep.* 5, 17405 (2015).
8. D. Bliss, V. Tassev, D. Weyburne, and J. Bailey, *J. Cryst. Growth* 250, 1 (2003).
9. Y. Kumagai, T. Yamane, and A. Koukitu, *J. Cryst. Growth* 281, 62 (2005).
10. Y. Katagiri, S. Kishino, K. Okuura, H. Miyake, and K. Hiramatu, *J. Cryst. Growth* 311, 2831 (2009).

11. H. Jeon, I. Jeon, G. Lee, S. Bae, H. Ahn, M. Yang, S. Yi, Y. Yu, Y. Honda, N. Sawaki, and S. Kim, *Jpn. J. Appl. Phys.* 56, 01AD07 (2017).

12. R. Schlesser, R. Dalmau, and Z. Sitar, *J. Cryst. Growth* 241, 416 (2002).

13. L.J. Schowalter, G.A. Slack, J.B. Whitlock, K. Morgan, S.B. Schujman, B. Raghothamachar, M. Dudley, and K.R. Evans, *Phys. Status Solidi C* 0(7), 1997 (2003). https://doi.org/10.1002/pssc.200303462.

14. B. Raghothamachar, R. Dalmau, B. Moody, H.S. Craft, R. Schlesser, J.Q. Xie, R. Collazo, M. Dudley, and Z. Sitar, *Mater. Sci. Forum* 717–720, 1287 (2012).

15. M. Bickermann, B. Epelbaum, O. Filip, P. Heimann, S. Nagata, and A. Winnacker, *Phys. Status Solidi C* 5, 1502 (2008).

16. P. Lu, R. Collazo, R. Dalmau, G. Durkaya, N. Dietz, B. Raghothamachar, M. Dudley, and Z. Sitar, *J. Cryst. Growth* 312, 58 (2009).

17. Z. Herro, D. Zhuang, R. Schlesser, and Z. Sitar, *J. Cryst. Growth* 312, 2519 (2010).

18. I. Nagai, T. Kato, T. Miura, H. Kamata, K. Naoe, K. Sanada, and H. Okumura, *J. Cryst. Growth* 312, 2699 (2010).

19. T. Kato, I. Nagai, T. Miura, H. Kamata, K. Naoe, K. Sanada, and H. Okumura, *Phys. Status Solidi C* 7, 1775 (2010).

20. C. Hartmann, A. Dittmar, J. Wollweber, and M. Bickermann, *Semicond. Sci. Technol.* 29, 084002 (2014).

21. H. Miyake, G. Nishio, S. Suzuki, K. Hiramatsu, H. Fukuyama, J. Kaur, and N. Kuwano, *Appl. Phys. Express* 9, 025501 (2016).

22. H. Miyake, C. Lin, K. Tokoro, and K. Hiramatsu, *J. Cryst. Growth* 456, 155 (2016).

23. R. Yoshizawa, H. Miyake, and K. Hiramatsu, *Jpn. J. Appl. Phys.* 57, 01AD05 (2018).

24. Online information. AlN substrate products of HexaTech, Inc., http://www.hexatechinc.com/aln-wafer-sales.html. Accessed 10 Nov 2019.

25. Online information. PIXcel3D x-ray Detector— Malvern PANalytical, https://www.malvernpanalytical.com/en/products/category/x-ray-components/detectors/pixcel3d. Accessed 12 Dec 2019.

26. P. Fewster and N. Andrew, *J. Appl. Crystallogr.* 28, 451 (1995).

27. M.A. Moram and M.E. Vickers, *Rep. Prog. Phys.* 72, 036502 (2009).

28. Y. Yao, Y. Ishikawa, Y. Sugawara, Y. Takahashi, and K. Hirano, *J. Electron. Mater.* 47, 5007 (2018).

29. Y. Yao, Y. Sugawara, Y. Ishikawa, N. Okada, K. Tadatomo, Y. Takahashi, and K. Hirano, *Jpn. J. Appl. Phys.* 58, SCCB29 (2019).

30. R. Chierchia, T. Böttcher, H. Heinke, S. Einfeldt, S. Figge, and D. Hommel, *J. Appl. Phys.* 93, 8918 (2003).

31. S.R. Lee, A.M. West, A.A. Allerman, K.E. Waldrip, D.M. Follstaedt, P.P. Provencio, D.D. Koleske, and C.R. Abernathy, *Appl. Phys. Lett.* 86, 241904 (2005).

32. W. Paszkowicz, S. Podsiadło, and R. Minikayev, *J. Alloys Compd.* 382, 100 (2004).

33. A.F. Wright, *J. Appl. Phys.* 82, 2833 (1997).

34. T. Damen, S. Porto, and B. Tell, *Phys. Rev.* 142, 570 (1966).

35. M. Kuball, J. Hayes, A. Prins, N. van Uden, D. Dunstan, Y. Shi, and J. Edgar, *Appl. Phys. Lett.* 78, 724 (2001).

36. A. Saura, M. Kuball, and J. Van Nostrand, *Appl. Phys. Lett.* 81, 1426 (2002).

37. H. Trodahl, F. Martin, P. Muralt, and N. Setter, *Appl. Phys. Lett.* 89, 061905 (2006).

38. V. Lughi and D. Clarke, *Appl. Phys. Lett.* 89, 241911 (2006).

39. S. Yang, R. Miyagawa, H. Miyake, K. Hiramatsu, and H. Harima, *Appl. Phys. Express* 4, 031001 (2011).

40. J. Wagner and F. Bechstedt, *Appl. Phys. Lett.* 77, 346 (2000).

41. D.B. Williams and C.B. Carter, *Transmission Electron Microscopy: A Textbook for Materials Science* (Berlin: Springer, 2009), pp. 323–345.

42. H.M. Foronda, A.E. Romanov, E.C. Young, C.A. Robertson, G.E. Beltz, and J.S. Speck, *J. Appl. Phys.* 120, 035104 (2016).

43. K. Ishiji, S. Kawado, Y. Hirai, and S. Nagamachi, *Jpn. J. Appl. Phys.* 56, 106601 (2017).

44. Online information. Sergey Stepanov's x-ray server, https://x-server.gmca.aps.anl.gov/index.shtml. Accessed 10 Nov 2019.

45. H. Matsuhata, H. Yamaguchi, I. Nagai, T. Ohno, R. Kosugi, and A. Kinoshita, *Mater. Sci. Forum* 600–603, 321 (2009).

46. H. Matsuhata, H. Yamaguchi, and T. Ohno, *Philos. Mag.* 92, 4599 (2012).

47. H. Yamaguchi, H. Matsuhata, and I. Nagai, *Mater. Sci. Forum* 600–603, 313 (2009).

48. X. Zhang, M. Skowronski, K.X. Liu, R.E. Stahlbush, J.J. Sumakeris, M.J. Paisley, and M.J. O'Loughlin, *J. Appl. Phys.* 102, 093520 (2007).

49. X. Zhang and H. Tsuchida, *J. Appl. Phys.* 111, 123512 (2012).